Optical Superlattice for Engineering Hubbard Couplings in Quantum Simulation

Thomas Chalopin[1,2,3,*], Petar Bojović[1,2], Dominik Bourgund[1,2], Si Wang[1,2], Titus Franz[1,2], Immanuel Bloch[1,2,4] and Timon Hilker[1,2]

[1]*Max-Planck-Institut für Quantenoptik, 85748 Garching, Germany*
[2]*Munich Center for Quantum Science and Technology, 80799 Munich, Germany*
[3]*Laboratoire Charles Fabry, Institut d'Optique Graduate School, CNRS, Université Paris-Saclay, 91127 Palaiseau, France*
[4]*Fakultät für Physik, Ludwig-Maximilians-Universität, 80799 Munich, Germany*

Quantum simulations of Hubbard models with ultracold atoms rely on the exceptional control of coherent motion provided by optical lattices. Here we demonstrate enhanced tunability using an optical superlattice in a fermionic quantum gas microscope, evidenced by long-lived coherent double-well oscillations, next-nearest-neighbor quantum walks in a staggered configuration, and correlated quantum walks of two particles initiated through a resonant pair-breaking mechanism. We furthermore demonstrate tunable spin couplings through local offsets and engineer a spin ladder with ferromagnetic and anti-ferromagnetic couplings along the rungs and legs, respectively. Our Letter underscores the high potential of optical superlattices for engineering, simulating, and detecting strongly correlated many-body quantum states, with direct applications ranging from the study of mixed-dimensional systems to fermionic quantum computing.

Introduction—Ultracold atoms confined in optical lattices have proven to be an exceptionally fruitful approach for exploring, understanding, and engineering quantum many-body phases [1]. During recent years, significant progress has been made in quantum simulations of Hubbard models, especially with quantum gas microscopes [2], which resolve individual particles of a degenerate quantum gas at each lattice site and allow manipulation of the quantum system with local control [3–11]. Lattices beyond the simple square geometry allow one to engineer different band structures [12–16], explore strongly correlated magnetic phases [17], simulate artificial magnetic fields and topology [18–21], prepare out-of-equilibrium states [22], implement quantum gates [23–27], induce frustration [28–30], and improve detection [31,32].

An optical superlattice consists of two (or more) superimposed optical lattices with commensurate lattice constants. Several types of implementations have been demonstrated in the context of quantum simulation: folded lattices [33], single-wavelength lattices [13], and bichromatic lattices [17,22,31,34–36]. A major challenge of such experimental platforms lies in achieving minimal phase noise for enhanced quantum coherence while maintaining a high degree of tunability for state engineering and dynamics. While state-of-the-art platforms have reported superlattice phase stability as low as 10 mrad [32,36], and even sub-mrad in tunable honeycomb lattices [37], practical implementations of exotic many-body physics in superlattice experimental platforms have been limited so far.

Here, we demonstrate enhanced state preparation, dynamics, and quantum simulation of the Fermi-Hubbard model with a bichromatic superlattice. We demonstrate a sufficiently high degree of control for novel applications, ranging from studying exotic Hubbard models to engineering building blocks of fermionic quantum computation. In particular, we implement double-well (DW) oscillations with substantial coherence times, strongly correlated quantum walks revealing direct control over nearest-neighbor (NN) and next-nearest-neighbor (NNN) coupling, and Fermi-Hubbard ladders with full control over spin super-exchange—including the inversion of its sign.

Description of the system—Our quantum simulator realizes the spin-$1/2$ repulsive Fermi-Hubbard model using ultracold ^{6}Li loaded in two-dimensional optical super-lattices generated from the interference of laser beams at 532 and 1064 nm under an angle of 26.7° [see Fig. 1(a)]. Our single-source bichromatic design ensures that the relative phase φ is robust to short-term drifts (see the End Matter for details regarding the implementation). The total potential $V(x, y)$ imprinted to the atoms takes the form
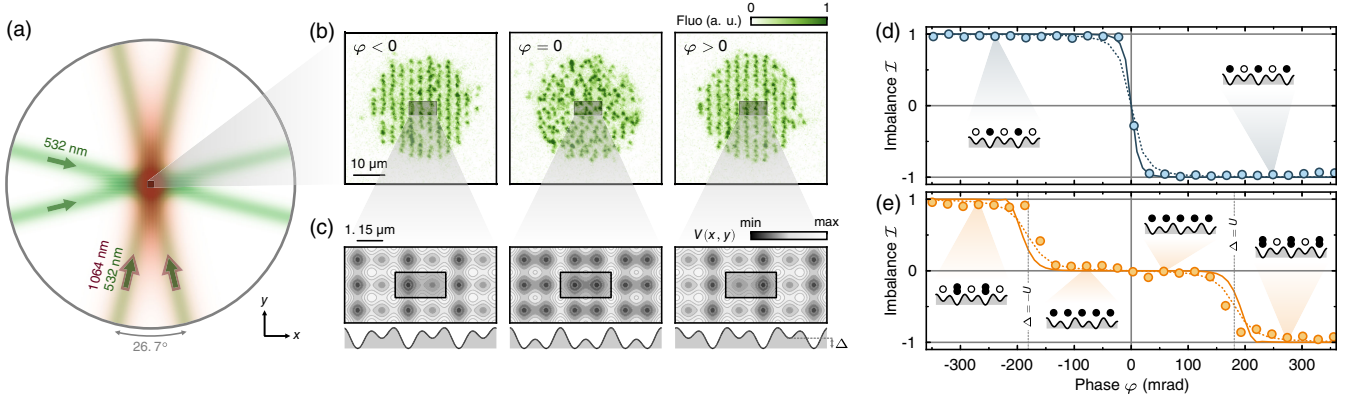
FIG. 1. Experimental setup. (a) The superlattice is engineered by superimposing optical lattices generated from the interference of laser beams at 532 and 1064 nm under an angle. In this Letter, only the short lattice (532 nm) is used in the y direction. (b) Exemplary site-resolved fluorescence pictures of atoms for different relative phases φ. (c) Lattice potential for the phases shown in (b), with the unit cell marked by the black rectangle. (d),(e) Imbalance $\mathcal{I}$ of the system in the case of (d) one atom or (e) two atoms per unit cell. The error bars in this figure, as in all other figures, are derived from a bootstrap procedure and are smaller here than the data points. The lines are obtained from the ground state of a two-site Fermi-Hubbard model with parameters t, U, and Δ (see the main text) obtained from *ab initio* Wannier function calculations with (solid lines) and without (dashed lines) accounting for the finite ramp time of our detection procedure [38].

$$V(x,y) = V_x\cos^2[\pi x/a_x + \varphi] + V_{x,\text{L}}\sin^2[\pi x/(2a_x)]$$
$$+ V_y\sin^2[\pi y/a_y], \tag{1}$$

where $a_x = 1.15(1)$ μm and $a_y = 1.11(1)$ μm are the lattice constants, V_x and V_y are the short lattice depths along x and y, $V_{x,\text{L}}$ is the long lattice depth along x, and φ is the relative phase. In the following, the lattice depths are expressed in units of their respective recoil energy $\text{E}_i^\text{R} = h^2/8ma_i^2$ ($i = x$, y) for the short lattices and $\text{E}_{x,\text{L}}^\text{R} = \text{E}_x^\text{R}/4$ for the long lattice, with h the Planck's constant and m the mass of a single atom.

The unit cell of the system contains two lattice sites, and the potential landscape within a unit cell varies continuously upon varying the phase φ. Staggered potentials with an energy offset on the even (odd) sites for $\varphi < 0$ ($\varphi > 0$) can thus be engineered, while a balanced configuration is obtained for $\varphi = 0$ [Fig. 1(c)]. The atomic ensemble is well described by the single-band Fermi-Hubbard model, with Hamiltonian

$$\hat{H} = \sum_{\langle ij\rangle,\sigma}\left[-t_{ij}\hat{c}^\dagger_{i,\sigma}\hat{c}_{j,\sigma} + \text{H.c.}\right] + U\sum_i \hat{n}_{i,\uparrow}\hat{n}_{i,\downarrow} + \sum_{i,\sigma}\Delta_i\hat{n}_{i,\sigma}, \tag{2}$$

where $\langle ij\rangle$ are NN sites, $\sigma = \uparrow,\downarrow$ is the spin state, $\hat{c}^\dagger_{i,\sigma}$ is the fermionic creation operator for spin σ at site i, t_{ij} is the tunnel coupling between sites i and j, $\hat{n}_{i,\sigma} = \hat{c}^\dagger_{i,\sigma}\hat{c}_{i,\sigma}$ is the atom number operator at site i for spin σ, $U > 0$ is the on-site interaction energy, and Δ_i is a site-dependent energy offset. In this Letter, $t_{ij} = t_y$ if i and j are NN along y, and $t_{ij} = t_x^{(1)}$ ($t_x^{(2)}$) for i and j NN along x within a unit cell

(between unit cells). The tunneling energies t_{ij} and offsets Δ_i are controlled by the lattice potential from Eq. (1), and the interaction energy between the two spin states, encoded by the lowest two hyperfine states of ^{6}Li, is set using the broad Feshbach resonance around 830 G. In the following, we describe single- and two-particle experiments involving engineered potentials such as isolated DWs and staggered configurations. Unless otherwise stated, we prepare a filling with an ensemble of both singly and doubly occupied isolated systems, on which single- and two-particle effects are identified via postselection, effectively exploring near-ground-state physics [45].

We measure the atomic density distribution with single-site resolution by performing fluorescence imaging [Fig. 1(b)]. We calibrate and characterize the lattice phase control of our apparatus by loading a balanced mixture of both spin states in the superlattice at different phases φ. The lattice depths are chosen in order to engineer a system of quasi-isolated DWs, with tunneling amplitudes in the balanced configuration $t_x^{(1)}/h = 510(73)$ Hz and $t_x^{(2)}/h = 13(1)$ Hz (see the End Matter). We measure the normalized imbalance $\mathcal{I} = (\langle\hat{n}_\text{o}\rangle - \langle\hat{n}_\text{e}\rangle)/(\langle\hat{n}_\text{o}\rangle + \langle\hat{n}_\text{e}\rangle)$ [Figs. 1(d) and. 1(e)], where $\langle\hat{n}_{\text{e(o)}}\rangle$ is the average atomic density on even (odd) sites. When considering DWs populated with a single atom [Fig. 1(d)], the symmetric phase $\varphi = 0$ is identified as the phase for which a balanced system ($\mathcal{I} = 0$) is engineered. As the phase changes, only the lowest well is populated in each unit cell, resulting in a strong shift in the imbalance toward $|\bar{\mathcal{I}}| = 0.985(2)$ in the large tilt regime 50 mrad $\leq |\varphi| \leq 300$ mrad $[4.3(6) \leq |\Delta/t_x^{(1)}| \leq 23(4)]$.

When considering DWs populated with two atoms, a fully imbalanced configuration is reached only for a tilt that

overcomes the interaction energy, $|\Delta_i| > U$. Thus, we observe a balanced configuration $\mathcal{I} = 0$ over a region $|\varphi| \lesssim \varphi_c$, with $\varphi_c \approx 170$ mrad in our system where $U/h \approx 7.7$ kHz, while a fully imbalanced configuration is reached for $|\varphi| \gtrsim \varphi_c$. In Figs. 1(d) and 1(e), the data are well matched by a ground-state calculation of a two-site Fermi-Hubbard model without free parameters.

Double-well oscillations—We highlight the single-particle control of our system by conducting DW oscillations. The system is initialized in a fully imbalanced configuration at $\varphi = -400$ mrad, here with about one atom per double well on average. Quenching the relative phase to $\varphi = 0$ at time $\tau = 0$ leads to an oscillation of the populations of the two sites in the double well [see Fig. 2(a)]. In our data analysis, we postselect on DWs containing exactly one detected atom.

The evolution is well captured by a resonant two-level oscillation with dephasing $\langle \hat{n}_L(\tau) \rangle = [1 + \cos(\omega\tau)e^{-\tau/\tau_d}]/2$. The extracted frequency $\omega = 2\pi \times 1.261(1)$ kHz is in good agreement with the expected frequency $\omega_{th} = 2t_x^{(1)}\hbar^{-1} = 2\pi \times 1.36(20)$ kHz calculated from the lattice depths (see the End Matter). Our apparatus furthermore allows one to probe DW oscillations locally, revealing spatial inhomogeneities in the oscillation frequency [Fig. 2(b)], which can be attributed to the inhomogeneities of the underlying

FIG. 2. Double-well oscillations. (a) Population evolution $\langle \hat{n}_L(\tau) \rangle$ on the left site of the DWs as a function of time τ after the quench ($\tau = 0$) from an imbalanced situation ($\varphi < 0$) to a symmetric double well ($\varphi = 0$). The orange point is used to evaluate our experimental π-pulse fidelity (see the text). (b) Local DW oscillation frequency. The black rectangle indicates the 22 DWs considered in (a). (c) Coherence of the measured oscillations (blue points) compared to different decoherence models (see the text).

lattice potential [38]. The decay time $\tau_d = 27(3)$ ms $= 33(4) \times 2\pi/\omega$ is found to be consistent with residual tunneling between neighboring DWs [Fig. 2(c)] owing to the finite depths of our lattices. Moreover, we find that this residual tunneling is the dominant source of decoherence compared to spatial inhomogeneities across the system and phase fluctuations (see the End Matter and the Supplemental Material [38]).

When the two-level system defined by the DW is interpreted as an orbital qubit [32], the quality of the oscillations directly indicates the fidelity of single-qubit operations. Specifically, we directly measure a π-pulse fidelity $P_\pi^{exp} = 1 - \langle \hat{n}_L(\tau = \pi/\omega) \rangle = 0.988_{-0.009}^{+0.007}$ [the orange point in Figs. 2(a) and 2(c)] by averaging over 22 DWs in the center of our system [the black rectangle in Fig. 2(b)]. Using the fit to the data, which takes into account dephasing and postselection (see above), we find that $P_\pi = 0.991(1)$. When taking into account the detection-induced errors associated with the motion and loss of particles during imaging, this fidelity increases to $P_\pi = 0.993(1)$ [38]. Because our primary source of decoherence is associated with inter-DW coupling, we expect the fidelity to improve if larger long lattice depths are achieved—in practice, we estimate $P_\pi > 0.999$ for reasonable depths $V_{x,L} \gtrsim 70 \, E_{x,L}^R$.

Quantum walks—We study larger-scale dynamics of our system via quantum walks in one dimension carried out in a standard ($V_{x,L} = 0$) and in a staggered ($V_{x,L} > 0$, $\varphi = \pi/2$, $t_x^{(1)} = t_x^{(2)} = t$) lattice potential. The system is initialized by populating a single column of atoms along y in a frozen configuration, and the dynamics along x is initiated at $\tau = 0$ by abruptly quenching the short and long lattices along x to lower depths (see the End Matter). The average atomic density $\langle \hat{n}_i(\tau) \rangle$ is then reconstructed as a function of space and time.

Figure 3(a) shows the dynamics of a single atom in a standard lattice. We postselect the experimental data on rows populated with one atom ($\sum_i \hat{n}_i = 1$), and we recover the expected dynamics from quantum walks [38]. The time axis is given in units of tunneling times $(\tilde{t}/\hbar)^{-1}$, where $\tilde{t}$ is an effective tunneling amplitude which, for standard lattices, is equal to the NN tunneling energy $\tilde{t} = t = h \times 96(11)$ Hz (see the End Matter). In a staggered potential [Fig. 3(b)], with $t/h = 320(25)$ Hz and an energy offset at neighboring sites $\Delta/h = 1.36(7)$ kHz, NN tunneling is almost completely suppressed. NNN sites, however, remain degenerate in energy, resulting in a nonzero effective coupling $\tilde{t} = t' + t^2/\Delta$. Here, $t'/h = -12(2)$ Hz is the direct tunneling process between the NNN sites, and $t^2/\Delta = h \times 76(13)$ Hz is a perturbative coupling that depends on the virtual population of the intermediate (NN) site [38]. In such a staggered configuration, the quantum walk is constrained to the sublattice that contains the initial state. Even in these slower dynamics, we observe coherent
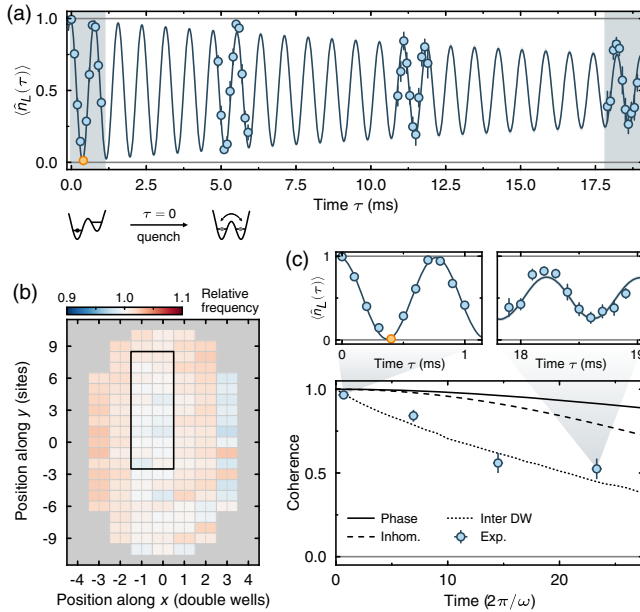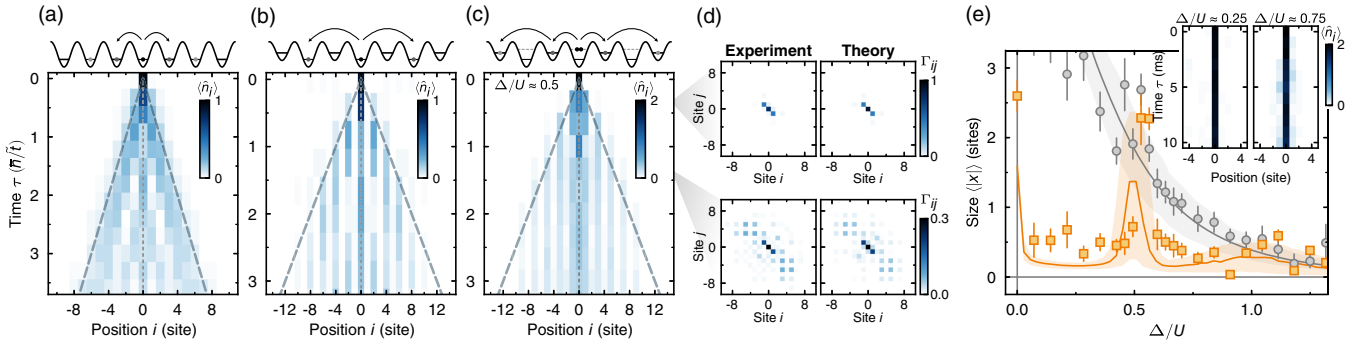
FIG. 3. Quantum walks on a superlattice. (a),(b) Symmetrized density distributions $\langle \hat{n}_i(\tau) \rangle$ for a state localized at $i = 0$ at $\tau = 0$ in the case of (a) a standard lattice and (b) a staggered superlattice at $\varphi = \pi/2$. In (a), the particle delocalizes on a timescale given by the NN tunneling energy $\tilde{t} = t = h \times 96(11)$ Hz. In (b), direct NN coupling is suppressed, but NNN processes remain resonant with an effective coupling $\tilde{t} = t^2/\Delta + t' = h \times 64(11)$ Hz (see the main text). (c) A superlattice initialized with a doublon features a resonant pair-breaking process upon tilting at $\Delta = U/2$, where the doublon is coupled to a delocalized state of two singly occupied neighbors. At longer times, the distribution behaves similarly to (b), with $\tilde{t} = t^2/(-\Delta) + t' = h \times 52(9)$ Hz. The dashed lines in (a)–(c) indicate the expected scaling behavior $x \sim 2\tilde{t}\tau/\hbar$ of the quantum walk expansion. (d) Correlation maps $\Gamma_{ij} = \langle \hat{c}_i^\dagger \hat{c}_j^\dagger \hat{c}_j \hat{c}_i \rangle$ of the experimental data and from numerical simulations. (e) Spatial extension of the density distribution after a fixed time $\tau = 4$ ms ($\tau t/\hbar \approx 8$, with t the bare tunnel coupling) as a function of the staggering offset Δ/U, and for singly and doubly occupied initial states (the gray circles and orange squares, respectively). The solid lines are obtained from numerical simulations, the shading indicating the uncertainty (1 standard deviation) resulting from the uncertainty of the Fermi-Hubbard parameters. Inset: examples of time evolutions of the density distribution where the resonant condition is not met showcase the absence of delocalization.

evolution up to almost ten sites before the expansion slows down due to large-scale inhomogeneities of our lattices inherent to the Gaussian envelope of the laser beams [38].

Interaction effects are revealed by postselecting data with two atoms per row ($\sum_i \hat{n}_i = 2$) and total spin 0, effectively considering dynamics with the initial state being a repulsively bound state [34,46,47], i.e., a doubly occupied site. In the staggered lattice considered here, the motion of the doublon is generally fully suppressed, as an NNN coupling would be a fourth order process in the tunneling energy [38]. However, a resonant pair-breaking process can be found by tuning the NN energy offset to be close to half the interaction energy, $\Delta = U/2$: the doublon at position $i = 0$ becomes degenerate with the state corresponding to one atom in each of the neighboring sites $i = \pm 1$, allowing a breaking of the bound pair. We show in Fig. 3(c) a quantum walk in this configuration, depicting population in sites $i = \pm 1$ in the early dynamics, as a consequence of this pair-breaking process. Subsequent dynamics appears to be similar to the one in Fig. 3(b), with a nonzero population on the sublattice that contains sites $i = \pm 1$. We probe correlations of the initially bound pair by evaluating the correlation map $\Gamma_{ij} = \langle \hat{c}_i^\dagger \hat{c}_j^\dagger \hat{c}_j \hat{c}_i \rangle = \langle \hat{n}_i \hat{n}_j \rangle - \langle \hat{n}_i \rangle \delta_{ij}$, with δ_{ij} the Kronecker delta. In Fig. 3(d), we show Γ_{ij} for two evolution times $\tau \tilde{t}/\hbar \approx 1$ and $\tau \tilde{t}/\hbar \approx 3.5$, revealing nonzero correlations between two atoms distant up to 12 sites for the latter. The agreement with theory is excellent [38], indicating that the quantum coherence of the evolution is maintained over a long time.

To highlight the striking difference between singly and doubly occupied initial states, we consider in Fig. 3(e)

the extension of the atomic density distribution $\langle |x| \rangle = \sum_i p_i(\tau)|x_i|$, with $p_i(\tau) = \langle \hat{n}_i(\tau) \rangle / \sum_i \langle \hat{n}_i(\tau) \rangle$, for a fixed time $\tau = 4$ ms ($t\tau/\hbar \approx 8$), as a function of the staggering energy offset Δ/U. For a singly occupied initial state (gray circles), we measure a localization of the distribution when increasing Δ, following the reduction of the effective tunneling energy $\tilde{t}$. For a doubly occupied initial state (orange squares), we observe a sharp resonance around $\Delta/U \approx 0.5$, corresponding to the pair-breaking situation of Fig. 3(c), while the distribution remains localized for most other staggering offsets (examples are given in the inset). At $\Delta = 0$, the extension of the atomic distribution is that of a bound pair in a standard lattice [47].

Engineering ferromagnetic couplings—While a staggered configuration allows tunneling to be suppressed, magnetic correlations are predicted to remain, except in the resonant configuration $\Delta \approx U$ for which a nonvanishing doublon population is expected [24,48]. Away from this resonant condition, NN spin interactions are expected to be described by a perturbative superexchange coupling J which changes sign for $\Delta > U$ (see the End Matter),

$$J(\Delta) = \frac{4t^2/U}{1 - (\Delta/U)^2}. \quad (3)$$

We explore this effect by loading an ensemble of ladders of length $L = 11$ with $\langle \hat{n} \rangle \approx 0.93$ atoms per site, with Hubbard parameters $t_x/h = 342(49)$ Hz ($t_y/h = 163(20)$ Hz) along the rungs (legs) and $U/h = 4.96(12)$ kHz at $\varphi = 0$ (see the End Matter). The loading procedure [Fig. 4(a)] relies on first freezing the system
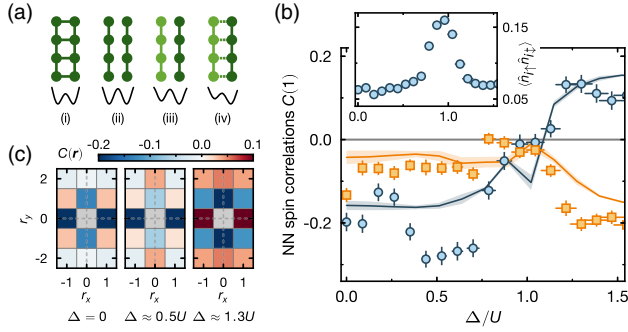
FIG. 4. Tuning the sign of the superexchange coupling. (a) The preparation sequence consists of four steps: (i) loading a balanced ladder configuration, (ii) decoupling the legs of the ladder, (iii) applying an offset Δ on one leg, and (iv) recoupling the legs. (b) NN spin correlations along x (blue) and y (orange) as a function of Δ. The solid lines are numerical results obtained from finite-temperature exact diagonalization (see the text). Inset: doublon density as a function of Δ. (c) Example of spin correlation maps illustrating the sign inversion of the spin coupling along x.

along x [steps (i) and (ii)] before applying the tilt with a variable superlattice phase φ [steps (iii) and (iv)] in order to prevent atoms from exclusively populating the lower leg in the regime of strong tilts $\Delta > U$. This procedure is very similar to the one used in our recent work [10,49] to engineer mixed-dimensional (mixD) systems. We evaluate the normalized spin-spin correlations,

$$C(\boldsymbol{r}) = \frac{1}{\mathcal{N}_{\boldsymbol{r}}} \sum_{\substack{i,j \\ i-j=r}} \frac{\langle \hat{S}_i^z \hat{S}_j^z \rangle - \langle \hat{S}_i^z \rangle \langle \hat{S}_j^z \rangle}{\sigma(\hat{S}_i^z) \sigma(\hat{S}_j^z)}, \qquad (4)$$

with $\sigma^2(\hat{S}_j^z) = \langle (\hat{S}_i^z)^2 \rangle - \langle \hat{S}_i^z \rangle^2$ the on-site spin fluctuations and $\mathcal{N}_{\boldsymbol{r}}$ a normalization constant counting the number of pairs of sites of size $\boldsymbol{r}$. We show in Fig. 4(b) the NN spin correlations $C(|\boldsymbol{r}| = 1)$ as a function of tilt Δ. The inset indicates the doublon density $\langle \hat{n}_{i\uparrow} \hat{n}_{i\downarrow} \rangle$, showing that an excess of doublons are created only in the vicinity of $\Delta \approx U$. The symmetrized spin correlation maps $C(\boldsymbol{r})$ are given in Fig. 4(c).

At $\Delta = 0$, the NN spin correlations are close to -0.2, with an asymmetry between the x and y directions due to the anisotropy of the superexchange coupling ($J_x/J_y \approx 4$). As Δ increases, J_x increases while J_y remains unchanged, resulting in an increase in the magnitude of the spin correlations along x and a slight decrease along y accounting for the redistribution of the correlations. The highest correlations are reached around $\Delta/U \approx 0.5$, in a regime where the rung tunneling is suppressed, while the doublon density remains low. Quite generally, for $\Delta < U$, we observe the characteristic checkerboard antiferromagnetic pattern, with strong rung singlets along x in the large J_x regime [Fig. 4(c)].

As Δ approaches U, we observe vanishing spin correlations in all directions, concomitant to the peak in the doublon density. When one tilts above the interaction energy $\Delta > U$, J_x changes sign, as expected from Eq. (3). In this regime, we observe positive spin-spin correlations along x, signaling ferromagnetic coupling along the rungs of the ladders, while antiferromagnetic ordering remains along y. The spin correlation map, which no longer features a checkerboard pattern, furthermore displays enhanced correlations along y due to the lack of competition in the spin ordering, as expected from the hybrid spin coupling engineered here.

The experimental data are compared to finite-temperature exact diagonalization of the Fermi-Hubbard model of Eq. (2) on a system of size 2×4 at half filling [38]. Our experimental results are qualitatively well reproduced by the numerical simulations [the solid lines in Fig. 4(b)], in which the different regimes realized in the experiment are identified: enhanced antiferromagnetic rung correlations for $0 < \Delta < U$, vanishing correlations around $\Delta \approx U$, and ferromagnetic rung correlations for $\Delta > U$. The quantitative differences, especially for rung correlations around $\Delta/U \approx 0.5$, are attributed to the finite size and finite doping effects of the numerical simulations [38]. Our simulations also suggest that the prepared states remain close to the equilibrium states of an effective mixD $t - J$ model without a drastic increase in temperature [38,49].

Conclusion—The different experiments conducted in this Letter, ranging from single-particle to many-body physics, illustrate how superlattices can be used in the context of quantum simulation using ultracold atoms. Our DW results can be extended to collisional gates [50,51] with the prospect of fermionic quantum computation [52–55], while the pair-breaking mechanism and correlated quantum walk regime [34,47,56] that we have demonstrated finds an application in the simulation of lattice gauge theories [57–59] and engineered quantum many-body systems [60]. We have shown how a superlattice can be used to control and modify the coupling strengths of the Hubbard Hamiltonian. Engineering ferromagnetic correlations in a many-body system at equilibrium, in particular, goes beyond previous work in DWs [24,61] and opens avenues for exploring symmetry-protected topological states [9].

Our Letter highlights the potential for the simulation of a broader range of real or theoretically interesting artificial materials. Specifically, our platform is well suited to exploring systems with mixed dimensionality [10,49,62–64], which appears to be crucial for novel types of unconventional superconductivity [65,66]. Superlattices and DW oscillations can reveal coherent pairing and superconducting order in quantum simulations of such systems [67].

[1] I. Bloch, J. Dalibard, and W. Zwerger, Rev. Mod. Phys. **80,** 885 (2008).

[2] C. Gross and W. S. Bakr, Nat. Phys. **17,** 1316 (2021).

[3] W. S. Bakr, J. I. Gillen, A. Peng, S. Fölling, and M. Greiner, Nature (London) **462,** 74 (2009).

[4] J. F. Sherson, C. Weitenberg, M. Endres, M. Cheneau, I. Bloch, and S. Kuhr, Nature (London) **467,** 68 (2010).

[5] C. Weitenberg, M. Endres, J. F. Sherson, M. Cheneau, P. Schauß, T. Fukuhara, I. Bloch, and S. Kuhr, Nature (London) **471,** 319 (2011).

[6] J.-Y. Choi, S. Hild, J. Zeiher, P. Schauß, A. Rubio-Abadal, T. Yefsah, V. Khemani, D. A. Huse, I. Bloch, and C. Gross, Science **352,** 1547 (2016).

[7] R. Islam, R. Ma, P. M. Preiss, M. E. Tai, A. Lukin, M. Rispoli, and M. Greiner, Nature (London) **528,** 77 (2015).

[8] G. Ji, M. Xu, L. H. Kendrick, C. S. Chiu, J. C. Brüggenjürgen, D. Greif, A. Bohrdt, F. Grusdt, E. Demler, M. Lebrat, and M. Greiner, Phys. Rev. X **11,** 021022 (2021).

[9] P. Sompet, S. Hirthe, D. Bourgund, T. Chalopin, J. Bibo, J. Koepsell, P. Bojović, R. Verresen, F. Pollmann, G. Salomon, C. Gross, T. A. Hilker, and I. Bloch, Nature (London) **606,** 484 (2022).

[10] S. Hirthe, T. Chalopin, D. Bourgund, P. Bojović, A. Bohrdt, E. Demler, F. Grusdt, I. Bloch, and T. A. Hilker, Nature (London) **613,** 463 (2023).

[11] A. W. Young, S. Geller, W. J. Eckner, N. Schine, S. Glancy, E. Knill, and A. M. Kaufman, Nature (London) **629,** 311 (2024).

[12] C. Becker, P. Soltan-Panahi, J. Kronjäger, S. Dörscher, K. Bongs, and K. Sengstock, New J. Phys. **12,** 065025 (2010).

[13] L. Tarruell, D. Greif, T. Uehlinger, G. Jotzu, and T. Esslinger, Nature (London) **483,** 302 (2012).

[14] G.-B. Jo, J. Guzman, C. K. Thomas, P. Hosur, A. Vishwanath, and D. M. Stamper-Kurn, Phys. Rev. Lett. **108,** 045305 (2012).

[15] L. Duca, T. Li, M. Reitter, I. Bloch, M. Schleier-Smith, and U. Schneider, Science **347,** 288 (2015).

[16] N. R. Cooper, J. Dalibard, and I. B. Spielman, Rev. Mod. Phys. **91,** 015005 (2019).

[17] M. Gall, N. Wurz, J. Samland, C. F. Chan, and M. Köhl, Nature (London) **589,** 40 (2021).

[18] M. Aidelsburger, M. Atala, S. Nascimbène, S. Trotzky, Y.-A. Chen, and I. Bloch, Phys. Rev. Lett. **107,** 255301 (2011).

[19] M. Lohse, C. Schweizer, O. Zilberberg, M. Aidelsburger, and I. Bloch, Nat. Phys. **12,** 350 (2016).

[20] S. Nakajima, T. Tomita, S. Taie, T. Ichinose, H. Ozawa, L. Wang, M. Troyer, and Y. Takahashi, Nat. Phys. **12,** 296 (2016).

[21] M. Lohse, C. Schweizer, H. M. Price, O. Zilberberg, and I. Bloch, Nature (London) **553,** 55 (2018).

[22] M. Schreiber, S. S. Hodgman, P. Bordia, H. P. Lüschen, M. H. Fischer, R. Vosk, E. Altman, U. Schneider, and I. Bloch, Science **349,** 842 (2015).

[23] M. Anderlini, P. J. Lee, B. L. Brown, J. Sebby-Strabley, W. D. Phillips, and J. V. Porto, Nature (London) **448,** 452 (2007).

[24] S. Trotzky, P. Cheinet, S. Fölling, M. Feld, U. Schnorrberger, A. M. Rey, A. Polkovnikov, E. A. Demler, M. D. Lukin, and I. Bloch, Science **319,** 295 (2008).

[25] B. Yang, H. Sun, C.-J. Huang, H.-Y. Wang, Y. Deng, H.-N. Dai, Z.-S. Yuan, and J.-W. Pan, Science **369,** 550 (2020).

[26] T. Hartke, B. Oreg, N. Jia, and M. Zwierlein, Nature (London) **601,** 537 (2022).

[27] W.-Y. Zhang et al., Phys. Rev. Lett. **131,** 073401 (2023).

[28] J. Yang, L. Liu, J. Mongkolkiattichai, and P. Schauss, PRX Quantum **2,** 020344 (2021).

[29] M. Xu, L. H. Kendrick, A. Kale, Y. Gang, G. Ji, R. T. Scalettar, M. Lebrat, and M. Greiner, Nature (London) **620,** 971 (2023).

[30] M. L. Prichard, B. M. Spar, I. Morera, E. Demler, Z. Z. Yan, and W. S. Bakr, Nature (London) **629,** 323 (2024).

[31] J. Koepsell, S. Hirthe, D. Bourgund, P. Sompet, J. Vijayan, G. Salomon, C. Gross, and I. Bloch, Phys. Rev. Lett. **125,** 010403 (2020).

[32] A. Impertro, S. Karch, J. F. Wienand, S. J. Huh, C. Schweizer, I. Bloch, and M. Aidelsburger, Phys. Rev. Lett. **133,** 063401 (2024).

[33] J. Sebby-Strabley, M. Anderlini, P. S. Jessen, and J. V. Porto, Phys. Rev. A **73,** 033605 (2006).

[34] S. Fölling, S. Trotzky, P. Cheinet, M. Feld, R. Saers, A. Widera, T. Müller, and I. Bloch, Nature (London) **448,** 1029 (2007).

[35] H.-N. Dai, B. Yang, A. Reingruber, X.-F. Xu, X. Jiang, Y.-A. Chen, Z.-S. Yuan, and J.-W. Pan, Nat. Phys. **12,** 783 (2016).

[36] M.-D. Li, W. Lin, A. Luo, W.-Y. Zhang, H. Sun, B. Xiao, Y.-G. Zheng, Z.-S. Yuan, and J.-W. Pan, Opt. Express **29,** 13876 (2021).

[37] M. N. Kosch, L. Asteria, H. P. Zahn, K. Sengstock, and C. Weitenberg, Phys. Rev. Res. **4,** 043083 (2022).

[38] See Supplemental Material at http://link.aps.org/supplemental/10.1103/PhysRevLett.134.053402, which includes Refs. [39–44], for details regarding sources of decoherence of our Rabi oscillations, an estimation of Hubbard parameters, and numerical simulations.

[39] J. Dalibard, Y. Castin, and K. Mølmer, Phys. Rev. Lett. **68,** 580 (1992).

[40] N. Marzari, A. A. Mostofi, J. R. Yates, I. Souza, and D. Vanderbilt, Rev. Mod. Phys. **84,** 1419 (2012).

[41] M. Modugno and G. Pettini, New J. Phys. **14,** 055004 (2012).

[42] U. Bissbort, Dynamical effects and disorder in ultracold bosonic matter, Ph.D. thesis, Goethe-Universität Frankfurt, Frankfurt, 2012.

[43] A. Polkovnikov, Ann. Phys. (Amsterdam) **326,** 486 (2011).

[44] A. Polkovnikov, K. Sengupta, A. Silva, and M. Vengalattore, Rev. Mod. Phys. **83,** 863 (2011).

[45] B. M. Spar, E. Guardado-Sanchez, S. Chi, Z. Z. Yan, and W. S. Bakr, Phys. Rev. Lett. **128,** 223202 (2022).

[46] K. Winkler, G. Thalhammer, F. Lang, R. Grimm, J. Hecker Denschlag, A. J. Daley, A. Kantian, H. P. Büchler, and P. Zoller, Nature (London) **441**, 853 (2006).

[47] P. M. Preiss, R. Ma, M. E. Tai, A. Lukin, M. Rispoli, P. Zupancic, Y. Lahini, R. Islam, and M. Greiner, Science **347**, 1229 (2015).

[48] L.-M. Duan, E. Demler, and M. D. Lukin, Phys. Rev. Lett. **91**, 090402 (2003).

[49] D. Bourgund, T. Chalopin, P. Bojović, H. Schlömer, S. Wang, T. Franz, S. Hirthe, A. Bohrdt, F. Grusdt, I. Bloch, and T. A. Hilker, Nature (London) **637**, 57 (2025).

[50] D. Jaksch, H.-J. Briegel, J. I. Cirac, C. W. Gardiner, and P. Zoller, Phys. Rev. Lett. **82**, 1975 (1999).

[51] T. Calarco, E. A. Hinds, D. Jaksch, J. Schmiedmayer, J. I. Cirac, and P. Zoller, Phys. Rev. A **61**, 022304 (2000).

[52] S. B. Bravyi and A. Y. Kitaev, Ann. Phys. (N.Y.) **298**, 210 (2002).

[53] P. Naldesi, A. Elben, A. Minguzzi, D. Clément, P. Zoller, and B. Vermersch, Phys. Rev. Lett. **131**, 060601 (2023).

[54] X. Sun, D. Luo, and S. Choi, arXiv:2306.03905.

[55] D. González-Cuadra, D. Bluvstein, M. Kalinowski, R. Kaubruegger, N. Maskara, P. Naldesi, T. V. Zache, A. M. Kaufman, M. D. Lukin, H. Pichler, B. Vermersch, J. Ye, and P. Zoller, Proc. Natl. Acad. Sci. U.S.A. **120**, e2304294120 (2023).

[56] J. Kwan, P. Segura, Y. Li, S. Kim, A. V. Gorshkov, A. Eckardt, B. Bakkali-Hassani, and M. Greiner, Science **386**, 1055 (2024).

[57] B. Yang, H. Sun, R. Ott, H.-Y. Wang, T. V. Zache, J. C. Halimeh, Z.-S. Yuan, P. Hauke, and J.-W. Pan, Nature (London) **587**, 392 (2020).

[58] Z.-Y. Zhou, G.-X. Su, J. C. Halimeh, R. Ott, H. Sun, P. Hauke, B. Yang, Z.-S. Yuan, J. Berges, and J.-W. Pan, Science **377**, 311 (2022).

[59] J. C. Halimeh, M. Aidelsburger, F. Grusdt, P. Hauke, and B. Yang, Nat. Phys. **21**, 25 (2025).

[60] M. Lebrat, A. Kale, L. H. Kendrick, M. Xu, Y. Gang, A. Nikolaenko, S. Sachdev, and M. Greiner, arXiv:2404.17555.

[61] K. Honda, S. Taie, Y. Takasu, N. Nishizawa, M. Nakagawa, and Y. Takahashi, Phys. Rev. Lett. **130**, 063001 (2023).

[62] F. Grusdt, Z. Zhu, T. Shi, and E. Demler, SciPost Phys. **5**, 057 (2018).

[63] A. Bohrdt, L. Homeier, I. Bloch, E. Demler, and F. Grusdt, Nat. Phys. **18**, 651 (2022).

[64] H. Schlömer, A. Bohrdt, L. Pollet, U. Schollwöck, and F. Grusdt, Phys. Rev. Res. **5**, L022027 (2023).

[65] H. Sun, M. Huo, X. Hu, J. Li, Z. Liu, Y. Han, L. Tang, Z. Mao, P. Yang, B. Wang, J. Cheng, D.-X. Yao, G.-M. Zhang, and M. Wang, Nature (London) **621**, 493 (2023).

[66] X.-Z. Qu, D.-W. Qu, J. Chen, C. Wu, F. Yang, W. Li, and G. Su, Phys. Rev. Lett. **132**, 036502 (2024).

[67] H. Schlömer, H. Lange, T. Franz, T. Chalopin, P. Bojović, S. Wang, I. Bloch, T. A. Hilker, F. Grusdt, and A. Bohrdt, PRX Quantum **5**, 040341 (2024).

[68] D. Bourgund, Charge correlations in quantum simulation of mixed-dimensional Hubbard systems, Ph.D. thesis, Ludwig-Maximilians-Universität München, 2024.

[69] A. Auerbach, *Interacting Electrons and Quantum Magnetism*, Graduate Texts in Contemporary Physics (Springer-Verlag, New York, 1994).

[70] A. B. Kuklov and B. V. Svistunov, Phys. Rev. Lett. **90**, 100401 (2003).

End Matter

Superlattice phase control and stability—The superlattice potential results from the superposition of two shallow-angle optical lattices produced from laser light at 532 and 1064 nm for the short and long lattices, respectively [Fig. 1(a)]. Each lattice is generated by the interference of two laser beams—the two *arms* of the lattice—with a difference in path length of about $L \approx 40$ cm. A change in the frequency of the laser field translates into a phase shift of the interference pattern as a consequence of this delay line. When the short lattice frequency is changed from $f = f_0 = c/(532 \text{ nm})$ to $f = f_0 + \Delta f$, with c the speed of light, the phase of the lattice potential changes by $\varphi = L\pi\Delta f/c$ [see Eq. (1)]. Experimentally, the frequency shift is induced by acousto-optic deflectors in a manner similar to that in [31]. In our setup, this method allows the relative phase φ to be tuned by $\sim 1.3\pi$, which is enough to go from a fully balanced configuration to a fully staggered configuration.

In the design process of the optical lattices, special care has been put into thermally and mechanically isolating the optical setup for splitting and recombining the lattice arms. The optical elements, in particular, are glued on a glass material with a low thermal expansion coefficient and placed in an evacuated box. The independent propagation in air of each arm is limited to about 10 cm. Additional details can be found in [68].

We evaluate the absolute phase stability of the setup through repeated measurements over several days. The absolute lattice phase, i.e., the absolute position of the lattice grid with respect to the acquisition camera, is inferred for each experimental realization. The results are given in Fig. 5(a) and illustrate the outstanding stability of our setup, featuring sub-lattice-site fluctuations over a period of more than two days.

The relative phase stability is inferred by performing repeated imbalance measurements [see Fig. 1(d)] in the balanced configuration ($\varphi = 0$). The average imbalance $\mathcal{I}$ is evaluated for each repetition and represented vs time in Fig. 5(b). Fluctuations of the imbalance around $\mathcal{I} = 0$ are attributed to the shot-to-shot fluctuation of the relative superlattice phase. In particular, we measure a standard deviation of the imbalance $\sqrt{\Delta\mathcal{I}^2} = 0.167$, corresponding to phase fluctuations $\sqrt{\Delta\varphi^2} \approx 4.5$ mrad according to the relation between imbalance and phase experimentally
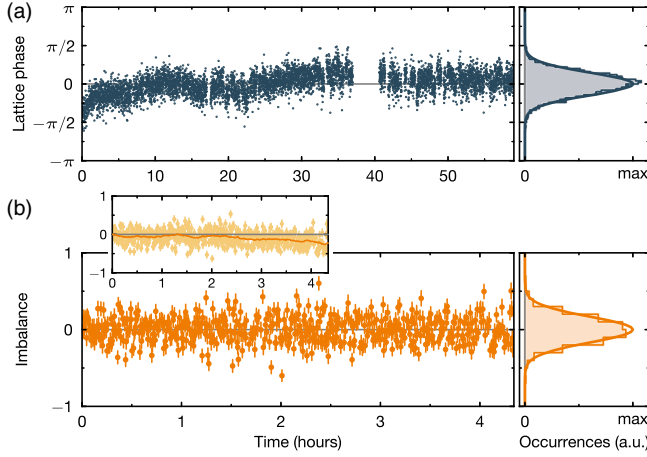
FIG. 5. Absolute and relative phase stability (a) Absolute phase measured over the course of more than two days. (b) Relative phase stability, inferred from the repetitive measurement of the average imbalance in the system over a few hours. Inset: shot-to-shot fluctuations extracted from the subtraction of long-term drifts and evaluated by a rolling average over a period of 20 min (solid orange line).

measured in Fig. 1 (thus already accounting for the effects of the freezing ramps). Note that these fluctuations are only slightly larger than what is expected from the shot noise $\sqrt{\Delta \mathcal{I}^2_{\text{shot}}} = 1/\sqrt{N}$ associated with the finite number of double wells considered here ($N = 66$). We also measure long-term drifts on timescales of several hours (inset). Over the course of data acquisition, these drifts are regularly compensated to ensure proper preparation of the system.

Experimental sequences—All our sequences start with a 2D degenerate Fermi gas with a balanced mixture of both spin states, loaded into a single fringe of a vertical

lattice with lattice constant $a_z = 3$ μm. In-plane confinement is ensured by a repulsive potential shaped by a digital micromirror device (DMD). The atomic density is controlled by varying the total atom number and the size of the in-plane confinement.

The atoms are then loaded into optical lattices, with the configurations varying depending on the specific experiment being performed. For the experiments presented in Figs. 2 and 3, the experimental procedure involves some dynamics initiated by quenching the superlattice relative phase or depth to a specified value (see below for details). For every sequence, the final step consists of freezing the atomic distribution by ramping up the short lattices to $V_i \approx 43$ E_i^R ($i = x, y$) in 1.5 ms before performing a spin-resolved fluorescence image of the system [31].

We give in Table I the lattice parameters for each of the measurements presented in this Letter. Additional information on the sequences are given below. More details on the calculation of the Hubbard parameters, can be found in the Supplemental Material [38].

Identification of the balanced configuration (Fig. 1): Before ramping up the lattice potentials, the relative phase φ is set to the value at which the measurement is performed. V_y and $V_{x,L}$ are then ramped up in 50 ms to their final value (see Table I), thus making a lattice with lattice constants $2a_x$ and a_y. After 5 ms of holding, V_x is ramped up to its final value in 50 ms, splitting each lattice site along the x direction in two. Freezing is performed after 2 ms of holding in the final configuration.

Double-well oscillations (Fig. 2): The relative phase φ is initialized to be far from the balanced configuration around -400 mrad. $V_{x,L}$ is ramped up first in 200 ms to its final value (see Table I), making 1D tubes separated by $2a_x$ along the x direction. After 20 ms of holding, both V_x and

TABLE I. Summary of experimental parameters. A range of parameters indicates that the parameter was varied during data acquisition. A blank cell indicates irrelevant parameters: the interaction strength for single-particle experiments and the relative phase when the long lattice is off.

Parameters	Unit	Figure 1	Figure 2	Figure 3(a)	Figure 3(b)	Figure 3(c)	Figure 3(e)	Figure 4
V_x	E_x^R	11.0(5)	10.0(5)	11.0(5)	6.0(3)	6.0(3)	6.0(3)	11.0(5)
$V_{x,L}$	$E_{x,L}^R$	31(1)	31(1)	0.0	1.00(5)	1.9(1)	[0, 4]	23(1)
V_y	E_y^R	40(2)	40(2)	40(2)	40(2)	40(2)	40(2)	9.0(5)
φ	mrad	$[-400, 400]$	0		$\pi/2$	$\pi/2$	$\pi/2$	[0, 240]
a_s	a_B	1293				973	973	1293
$t_x^{(1)}/h$	Hz	510(73), 604(97)[a]	675(101)	97(13)	320(25)	323(25)	334(27)[b]	342(49), 349(51)[c]
$t_x^{(2)}/h$	Hz	13(1), 19(2)[a]	14(1)	96(11)	320(25)	323(25)	334(27)[b]	22(2), 24(2)[c]
t_y/h	Hz	< 1	< 1	< 1	< 1	< 1	< 1	163(20)
t'/h	Hz	< 1	< 1	< 1	12(2)	14(2)	16(3)[b]	< 1
U/h	kHz	7.53(16), 7.84(15)[a]				4.83(1)	4.88(10)[b]	4.96(12), 5.04(11)[c]
Δ/h	kHz	0, 16.7(5)[a]				2.58(14)	5.43(27)[b]	0, 7.66(32)[c]

[a]Values for $\varphi = 0$ and 400 mrad, respectively.
[b]Values for $V_{x,L} = 4.0(2)$ $E_{x,L}^R$.
[c]Values for $\varphi = 0$ and 240 mrad, respectively.

V_y are ramped up to their final values in 200 ms. Such a procedure allows, on average, one atom per double well to be loaded, assuming that the overall density is well set and the interaction strength is large enough. The lattice depths are held at these values for 20 ms before freezing. The double-well oscillations are triggered by quenching the relative phase φ to the balanced configuration in 45 μs at a time $\tau \in (0\,\text{ms}, 20\,\text{ms}]$ before freezing. The freezing procedure, in this case, also involves quenching φ back to the initial phase. The data point at $\tau = 0$ ms is taken without quench.

Quantum walks (Fig. 3): For each of the quantum walk experiments, a tailored DMD potential restricts the system size to a single row of lattice sites along y, which is identified as position $x = 0$. V_y and $V_{x,\text{L}}$ are ramped up together in 200 ms to about 40 E_y^R and 31 $\text{E}_{x,\text{L}}^\text{R}$, thus making a single 1D array of atoms. Only then is the short lattice turned on, as V_x is ramped up to 40 E_x^R in 200 ms. This two-step procedure facilitates initial state preparation, as loading a single array of atoms in the long lattice is easier than directly loading the short lattice. The relative phase is always initialized beforehand to the configuration with maximum contrast ($\varphi = \pi/2$), which ensures that all the population of a single long lattice site is transferred to a single short lattice site upon ramping up V_x. The system is held frozen for 9 ms before $V_{x,\text{L}}$ is ramped down to its final value (see Table I) in 20 ms. The dynamics is triggered by quenching V_x to its final value in 1 ms. The end of the quench ramp marks the beginning of the evolution of duration τ before freezing, and the data at $\tau = 0$ ms are acquired without quench.

Ferromagnetic ladders (Fig. 4): The relative phase is initialized in the balanced configuration $\varphi = 0$. Then, all the lattices are ramped up in 250 ms, going through configurations (i) and (ii) in Fig. 4(a). The intermediate lattice depths after step (ii) are $V_x \approx 30\,\text{E}_x^\text{R}$, $V_{x,\text{L}} = 23(1)\,\text{E}_{x,\text{L}}^\text{R}$, and $V_y \approx 7\,\text{E}_y^\text{R}$. The tilt is applied by quenching the relative phase φ to its final value in 0.5 ms. The short lattices are then ramped to their final value (see Table I) in 45 ms. Freezing is performed after 0.5 ms in this final configuration.

Superexchange in tilted double wells—The DW Hamiltonian in the presence of a tilt Δ reads

$$\hat{H}_{\text{DW}} = -t\big(\hat{c}_{L,\uparrow}^\dagger \hat{c}_{R,\uparrow} + \hat{c}_{L,\downarrow}^\dagger \hat{c}_{R,\downarrow} + \hat{c}_{R,\uparrow}^\dagger \hat{c}_{L,\uparrow} + \hat{c}_{R,\downarrow}^\dagger \hat{c}_{L,\downarrow}\big)$$
$$+ U\big(\hat{n}_{L,\uparrow}\hat{n}_{L,\downarrow} + \hat{n}_{R,\uparrow}\hat{n}_{R,\downarrow}\big) + \Delta\big(\hat{n}_{R,\uparrow} + \hat{n}_{R,\downarrow}\big).$$

We consider here the case of two atoms in total with opposite spins that are well described by the Fock basis $|\uparrow,\downarrow\rangle, |\downarrow,\uparrow\rangle, |\downarrow\uparrow,0\rangle, |0,\downarrow\uparrow\rangle$. In the limit $U \gg \Delta, t$, the energy spectrum separates into two manifolds, with low-lying states $\mathcal{E}_s = \{|\uparrow,\downarrow\rangle, |\downarrow,\uparrow\rangle\}$ (singly occupied sites) forming the ground-state manifold, and higher energy states $\mathcal{E}_d = \{|\downarrow\uparrow,0\rangle, |0,\downarrow\uparrow\rangle\}$ (the presence of doubly occupied sites). Although $\hat{H}_{\text{DW}}$ does not directly couple the two states within $\mathcal{E}_s$, a second-order perturbation calculation leads to an effective coupling within this manifold [69,70] described by an effective Hamiltonian $\hat{H}_{\text{DW}}^{\text{eff}} = J\hat{\mathbf{S}}_{\text{L}} \cdot \hat{\mathbf{S}}_{\text{R}}$, where $J = 2t^2/(U-\Delta) + 2t^2/(U+\Delta)$ is the superexchange coupling (3). Such an effect is well understood by considering that both states of $\mathcal{E}_s$ are coupled by the virtual population of $\mathcal{E}_d$, with energies $U - \Delta$ and $U + \Delta$. This situation is illustrated in Fig. 6(a).

In the case where $\Delta > U$ but $\Delta - U \gg t$, such that $\mathcal{E}_s$ remains well separated in energy from $\mathcal{E}_d$, the expression remains valid, even though $\mathcal{E}_s$ does not constitute a ground-state manifold anymore. This situation is illustrated in Fig. 6(b).
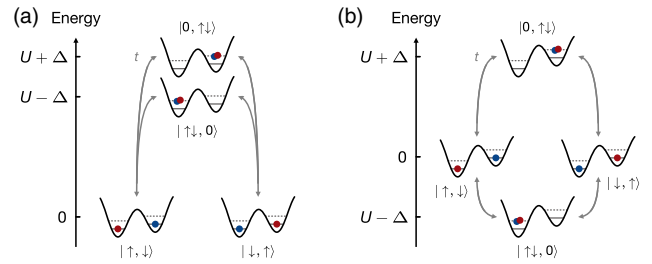

FIG. 6. Inversion of spin superexchange (a) Energy manifolds for $\Delta \ll U$. (b) Energy manifolds for $\Delta > U$. In both cases, degenerate states with single occupancies ($|\uparrow,\downarrow\rangle$ and $|\downarrow,\uparrow\rangle$) are perturbatively coupled by virtual population of states with double occupancies ($|\uparrow\downarrow,0\rangle$ and $|0,\downarrow\uparrow\rangle$).